Journal of Power Sources 204 (2012) 265–272

Contents lists available at SciVerse ScienceDirect

Journal of Power Sources

journal homepage: www.elsevier.com/locate/jpowsour

Characterization of TiO_2 nanotubes obtained by electrochemical anodization in organic electrolytes

S. Palmas[a,*], A. Da Pozzo[a], F. Delogu[a], M. Mascia[a], A. Vacca[a], G. Guisbiers[b]

[a] Dipartimento di Ingegneria Chimica e Materiali, Università di Cagliari, Piazza D'armi, 09123 Cagliari, Italy
[b] Institute of Mechanics, Materials and Civil Engineering, Louvain Catholic University, Place Sante Barbe 2, 1348 Louvain-La-Neuve, Belgium

ARTICLE INFO

Article history:
Received 8 September 2011
Received in revised form
10 November 2011
Accepted 1 January 2012
Available online 8 January 2012

Keywords:
Photoelectrocatalysis
TiO_2 nanotubes
Glycerol
Ethylene glycol
Electrochemical impedance spectroscopy
Water splitting

ABSTRACT

TiO_2 nanotubular structures were prepared by electrochemical oxidation performed in organic electrolytes containing fluorides protracted up to different times. After the annealing treatment, required to obtain crystalline structures, samples were submitted to morphological, electrical and photoelectrochemical analysis.

The obtained results suggest that in the presence of porous structures such as nanotube arrays the photo catalytic behaviour of the samples cannot be simply explained considering the different specific areas, but also the electronic properties of the electrodes have to be taken into account.

Electrochemical impedance spectroscopy was used to correlate the morphology of these structures with their electronic properties and their working mechanism in the presence of a light radiation.

A schematic representation of the nanotube structures as consisting of two layers, compact and porous, proved to be appropriate to clarify the obtained results.

1. Introduction

Titanium dioxide is a well known semiconductor material: its photocatalytic properties, especially in the range of UV wavelengths, gave rise to such a high number of scientific works, that citation of all the related papers which have appeared in the literature is very difficult. Wide-ranging work has been carried out by several research groups, such those of Fujishima et al. [1], Macak et al. [2], Grimes and co-workers [3], just to cite some recent reviews. Despite this, more questions are still open and several efforts are addressed to modify the titania structure to extend its activity in the range of visible radiation [4–6]. In this contest, the full understanding of the system as well as the modelling of a possible working mechanism of the structure still constitute important starting points to engineering photoactive catalysts. In order to give a contribution in this direction, the present work is addressed to the study of the behaviour of titania nanotubular arrays in the range of near visible light.

As it is well known, the electrical and photo-electrical properties of titania are determined by its non-stoichiometry and the related concentration of point defects in the lattice [7,8]. The non-stoichiometry is determined by the apparent deficit of oxygen: accordingly, the correct formula of titanium dioxide is TiO_{2-x} where x is determined by the concentration of ionic lattice defects. Oxygen vacancies and Ti interstitials have been considered as predominant donor defects [8]. However, it has been recently shown [9,10] that also Ti vacancies formed at the surface and subsequently transported to the bulk during the oxidation of TiO_2, play a crucial role in photoreactivity between TiO_2 and H_2O, being the only acceptor-type intrinsic defects in undoped TiO_2 [10].

All these localized states can act as recombination sites (shallow traps) or trap filling sites (deep traps) [11], influencing the photoactivity of the titania. Moreover, when TiO_2 nanotubular structures are concerned, these states can be differently located between the compact base oxide layer and the porous overlayer [12]. There are many factors that can determine a different distribution of such defects in these structures: a recent study [13] has shown that differences in the anodization curves can be related with different distributions of defects within the structures and that these defects are differently sensitive to the annealing treatment. In particular, a higher surface area and higher concentration of superficial electronic defects, more sensitive to temperature, can be expected in the porous overlayer compared to the base oxide.

The presence of multiple donor levels in nanotube structures can be highlighted by the analysis of Mott Schottky (MS) that shows variable slopes and high dispersion of data with the frequency. In the ideal condition in which there are no intragap states, a linear trend in the MS plot is expected: the application of a positive potential moves the electrons away from the charge space region increasing the depletion and thus decreasing its capacity.

* Corresponding author. Tel.: +39 0706755069; fax: +39 0706755067.
E-mail address: sipalmas@dicm.unica.it (S. Palmas).

0378-7753/$ – see front matter © 2012 Elsevier B.V. All rights reserved.
doi:10.1016/j.jpowsour.2012.01.007

Table 1
Experimental conditions of anodization for the considered samples. All the anodization were performed at 20 V.

Sample	Anodization time	Anodization bath
G1	1 h	Glycerol 75%, water 25%, [F⁻] = 0.14 M
G3	3 h	
G9	9 h	
EG1	1 h	Ethylene glycol 98%, water 2%, [F⁻] = 0.14 M
EG3	3 h	
EG9	9 h	

When intragap states are present, they are emptied by the applied potential passing through their energetic levels. During this empting process, the Fermi level is pinned and the band bending (and thus the capacity) is independent of the applied potential. Moreover, when the applied potential is more positive than the intragap states, the excess of positive charges accumulated at these emptied states shifts the flat band potential to the positive direction decreasing the depletion and thus changing the slope in MS plot [14]. The wide variation of data with frequency is just related to the rate of the ionization of the states, in turn dependent on their energetic position inside the band gap [15]. The impedance measurement can detect the presence of intragap states only if the frequency of oscillation of the applied potential is lower than their emptying rate. Hence, at high frequencies only the contribution of superficial and fast states is visible, whereas at lower frequencies also the contribution of slower and deep states can be detectable.

Changing the selected operative conditions in the preparation of the samples (electrolyte, water content, anodization time) can significantly influence their morphology and electronic structure. The study carried out is aimed at assessing whether and in which extent these changes can influence the electronic properties of nanotube layers and thus the effectiveness of the photo-catalytic process.

2. Experimental

2.1. Electrochemical cell

A three electrode cell was used in all the electrochemical and photo-electrochemical experiments, in which a platinum grid worked as counter electrode and a saturated calomel electrode (SCE) as reference. All the values of potential in the text are referred to SCE. All the experiments were carried out at the temperature of 20 °C kept constant by water cool recirculation. A potentiostat AMEL 7050 controlled by JuniorAssist software, has been employed for all the electrochemical studies.

2.2. Preparation of the electrodes

Ti foils (0.25 mm thick, 99.7% metal basis, Aldrich) were used as starting material to obtain the 1 cm^2 TiO_2 photoelectrodes according to a previously reported procedure [12,13]. After a preliminary degreasing treatment, the samples were submitted to electrochemical anodization, performed in glycerol or ethylene glycol solutions containing different amount of water and fluoride ions (Table 1). A potential ramp was applied from open-circuit voltage (OCV) to a fixed potential (20 V) with a scan rate of 100 mV s^{-1}; then, the applied potential was maintained at this fixed value for different times. After oxidation, the electrodes were rinsed in deionized water and dried in a nitrogen stream. A subsequent annealing treatment was needed in order to transform the amorphous into crystalline structure. Thermal treatments were performed in air atmosphere for 1 h at 400 °C.

Table 2
Average values of diameters and wall thickness of the considered samples: the values have been calculated by analyzing 10 nanotubes on each picture. The error bar is calculated by maximizing the difference between the average value and the experimental value.

Sample	Diameter of the tubes (nm)	Wall thickness (nm)
G1	131 ± 21	31 ± 4
G3	142 ± 31	36 ± 8
G9	157 ± 49	37 ± 13
EG1	71 ± 13	17 ± 4
EG3	82 ± 12	18 ± 4
EG9	89 ± 15	22 ± 6

2.3. Characterization of the electrodes

Scanning electron microscopy (SEM) was used to study the morphology of the assembled electrodes. SEM measurements were performed by a FE-SEM Zeiss Ultra 55 working in the high vacuum mode (accelerating voltage = 1 kV, WD ~ 4–5 mm).

Absorption spectra were obtained by using a Cary 5E UV–vis–NIR spectrophotometer from Varian. The scan registered the absorption of each sample on the wavelength range: 190–800 nm. The baseline has been calibrated with a white reference sample. The software used to analyse the data was CaryWinUV Scan Application delivered with the spectrometer (1999).

In the photocurrent experiments the TiO_2 sample was submitted to a potential ramp from its open circuit potential (OCV) to about 1.2 V, at a constant scan rate of 5 mV s^{-1}, in the dark and under illumination. The value of photocurrent density was taken as the difference between light and dark currents.

The light source was a 300 W Xe lamp (Lot Oriel): the behaviour of the samples was studied using a filter with centre wavelength at 380 nm (band width 10 nm). The average light intensity striking on the surface of the electrodes was measured by a photo radiometric sound (Delta Ohm HD 2302.0) and it was 6 mW cm^{-2}. Photocurrents were normalized with respect to incident light power.

Electrochemical impedance spectroscopy (EIS) measurements were carried out in absence and in presence of light source, at different bias potentials for each sample. A frequency response analyser (FRA, Model 7200 AMEL) was used to perform these experiments in a frequency range from 100 kHz to 0.1 Hz. The capacitance values C_{SC} at the different potentials were derived by the imaginary part of the impedance evaluated at each frequency. The value of the donor density (N_D) was calculated from the slope of the linear part of the plot reporting $1/C_{SC}^2$ vs the applied potential.

A voltammetric analysis was performed in order to derive the active surface areas of the samples: cyclic voltammetry (CV) measurements were performed between 0 and 0.5 V at different scan rates (10–500 mV s^{-1}). The current densities were calculated using the apparent geometric area of the electrodes (1 cm^2).

All the experiments were carried out in 0.1 M KCl aqueous solution.

3. Results and discussion

Table 1 summarizes the operative conditions adopted in preparing the different samples. In the following, samples grown in glycerol solution will be called G samples, while those grown in ethylene glycol will be called EG samples; in both the cases the associate number indicates the anodization time expressed in hours.

Fig. 1 shows some examples of SEM images of the obtained samples. Samples G exhibit a more regular structure than samples EG, at which an increasing disorder is detected at higher anodization times, probably due to the collapse of the nanotubes.

An analysis of all the SEM images related to each kind of samples, allowed us to estimate the mean values of diameter and wall

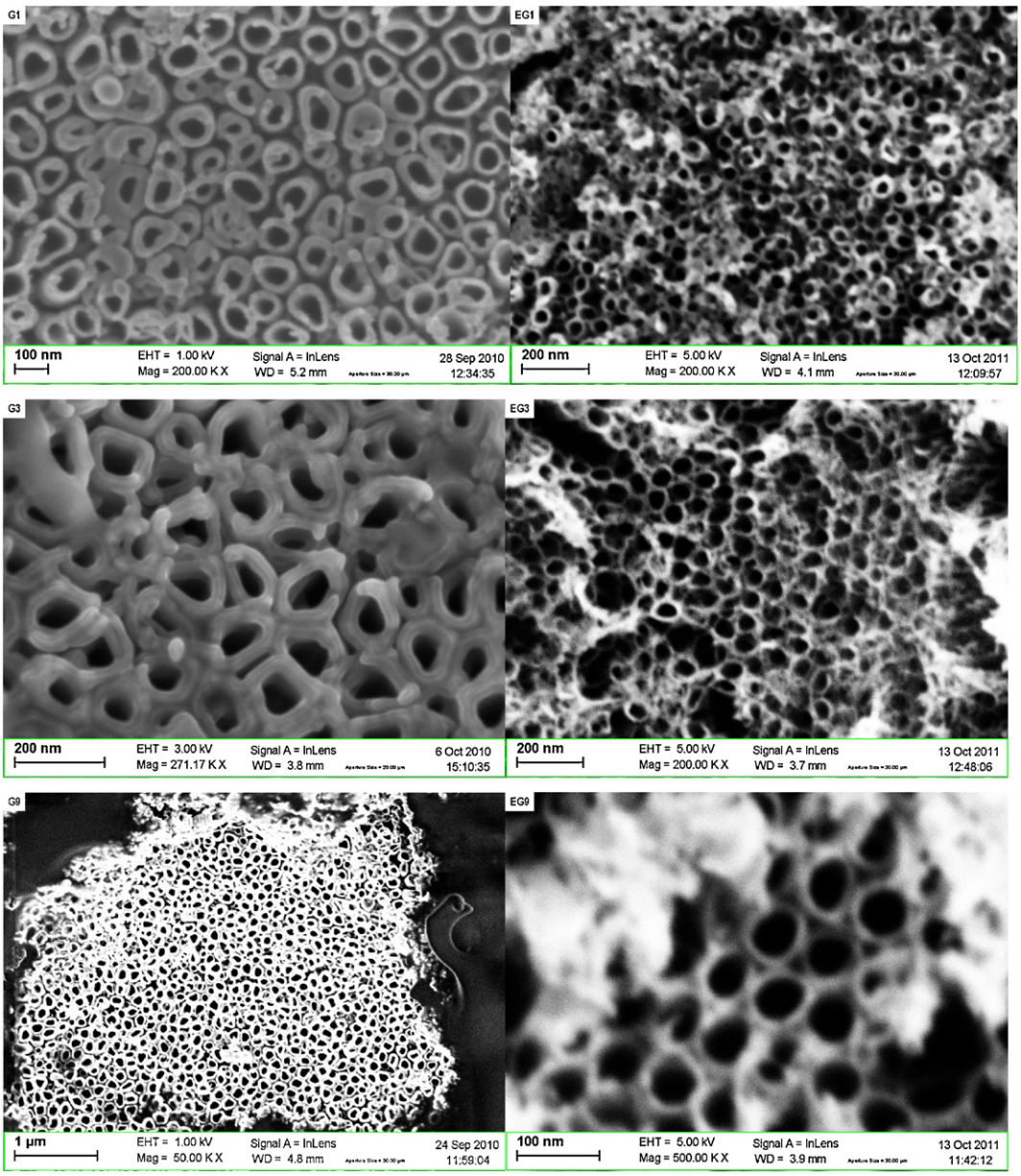

Fig. 1. SEM images of the investigated samples.

thickness of the nanotubes: the relevant values have been calculated by analysing 10 nanotubes on each picture, and the error bar is calculated by maximizing the difference between the average value and the experimental value. As resumed in Table 2, the values related to samples produced in glycerol/water based electrolyte seems to be higher than those growth in ethylene glycol/water based electrolyte: this fact can be due to the different electrolyte and also, as reported in the literature, to the different water content [16].

Always literature indicates a higher growth rate of nanotubes in ethylene glycol because of the lower viscosity and the lower water content [17–19]. Also, more regular structures could be obtained in ethylene glycol using higher anodization potentials [20]: in the present case the low potential applied during the anodization could be the reason for the disorder in the structure. Nevertheless, as shown in the following, this fact seems to not affect the photo activity of the samples, also due to the obtained large surface areas.

As the photo-activity of the samples is concerned, Fig. 2 shows the absorption spectra of the samples investigated.

As we expected, all the samples show good absorption capacity in the UV range, with absorption peaks in the UV-B (280–315 nm) and UV-C (200–280 nm) but, due to our interest to possible applications in the visible range, in the present case the attention has been focused on the UV-A range (315–400 nm); in particular, the performance of the samples have been investigated around the minimum in the absorption spectrum. To this aim, the curves of photocurrent versus the applied potential, have been obtained at the incident light wavelength of 380 nm.

Fig. 3 reports the results obtained at the different samples, normalized with respect to incident light power. As it can be seen, the shapes of the photocurrents are quite different: the electrodes grown in glycerol exhibit trends highly dependent on the potential and the saturation value is not reached, at least in the investigated potential range; on the contrary, the electrodes grown in ethylene glycol show curves that, after a few mV, reach a saturation

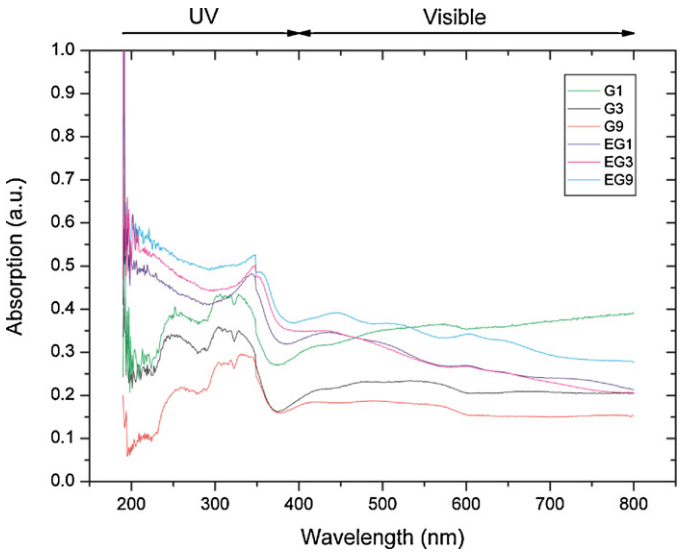

Fig. 2. Absorption spectra of the investigated samples.

value at which the current density does not depend on the applied potential. Anodization time appears much more effective at electrodes grown in ethylene glycol than at those grown in glycerol. Furthermore, photocurrents obtained at EG anodes are generally higher than at G samples.

In order to explain these results a further characterization of the samples was performed accounting for both the morphologic and electronic structure of the samples. Actually, as suggested in literature [21], when semiconducting nanotubular structures are concerned, the photo-activity of the samples may be determined by a combined effect of the extent of the active surface area and of the electronic structure of the semiconductor material.

3.1. Surface area characterization

Cyclic voltammetries (CVs) carried out at different scan rates allow to estimate the total charge associated to the sample as the sum of the outer charge and the inner one, related to different accessibility of the electrolyte [22]. The total voltammetric charge (q_{TOT}) is related to the real surface area but is also affected by the specific electroactivity of the electrodes. So, a range of potential between 0 and 0.5 V where no faradic currents occurred, was chosen to estimate the real surface area. In this potential range CV were performed at scan rates in the range from 10 to 500 mV s^{-1} and total voltammetric charges were studied as function of the scan rate.

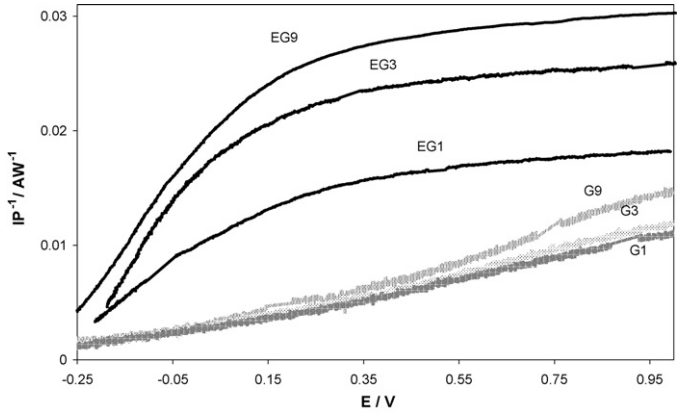

Fig. 3. Trend of photocurrents (normalized to incident power light) vs potential, for the investigated samples. λ = 380 nm.

Based on this analysis, the extrapolation of q to $\nu = 0$ from $1/q$ vs. $\nu^{0.5}$ curves gives the total voltammetric charge (q_{TOT}); the extrapolation of q to $\nu = \infty$ from the q vs $\nu^{-0.5}$ curves gives the outer voltammetric charge (q_{OUT}), connected to the most accessible surface. The inner voltammetric charge (q_{IN}), that corresponds to the less accessible surface sites of the oxide layer, can be calculated by difference. Fig. 4 plots the values of total, outer and inner charges for the studied samples.

The results show that in all the cases G electrodes have lower total charges, which can be connected to lower superficial areas. For G electrodes the total area is almost equal to the external one, indicating that the electrolyte can exploit almost all the surface. However, the order of magnitude of the charge for G samples is very low, and also it seems to be not worthy to carry out the oxidation for more than 3 h because the low relative increase in the charge.

On the other hand EG electrodes show a large increase in the total charge with the anodization time, that could support the higher growth rate. The external charge is not coincident with the total one, indicating in the case of EG electrodes a minor accessibility for the electrolyte, as could be inferred from SEM analysis and in agreement with the smallest values of the tube diameters. However, an increase in the anodization time from 3 to 9 h does not seem to lead to a further loss in the accessible surface.

Nevertheless, the photo catalytic behaviour of the samples cannot be simply explained considering the different areas: surface area ratios of 1:1.7:2, and 1:15:25 for G and EG samples respectively was derived at 1:3:9 h, which are not proportional with the increasing ratios of photocurrents at the relative electrodes: their values measured at 0.6 V were in the order 1:1.1:1.2 for G electrodes and 1:1.5:1.6 for EG electrodes.

So, a further analysis on the electronic properties of the electrodes has to be taken into account.

3.2. Electronic characterization

EIS analysis was performed either in the dark or under irradiation, in order to investigate on the electronic structure of the samples, and on their working mechanism.

An example of the obtained results in terms of Nyquist plot is reported in Fig. 5: in agreement with the results from photocurrent tests, the impedances recorded at EG sample are lower than those at G sample. Bode plots of modulus and phase angle are also reported in Fig. 6 along with the equivalent circuit which was able to interpret well the data. As already stated with analogous samples [12,15], the behaviour of the nanotubular samples can be described as the consequence of a two-film structure conformed by a compact base layers, constituted by the oxide film not interested by the nanotubular structure, and a porous overlayer, where nanotubes are fully developed. Thus, two RQ elements are needed in the equivalent circuit, to take into account for the capacitive-resistive processes occurring at the interface of the two layers. Actually, constant phase elements are used in this case instead of pure capacitors for a better agreement with experimental data: their admittance is expressed by $Y = Q(j\omega)^n$, being $n = 1$ for perfect capacitors. The behaviour of the porous layer is associated in this model to the RQ circuit element presenting the lowest value of resistance: values of the exponent n quite different from 1 are obtained at this element, indicating a strong deviation from the ideal behaviour of capacitors and the possible presence of diffusive effects. The RQ circuit element with higher resistance has been associated to the compact layer: a behaviour closer to the ideal capacitor is indicated by the exponent n closer to 1.

The resistance R_1, in all the cases around 30–40 Ω cm^2, takes into account the external and the solutions resistances. All the circuit parameters obtained for compact and porous layers are reported in Table 3. On these bases, a different superficial area, as well a

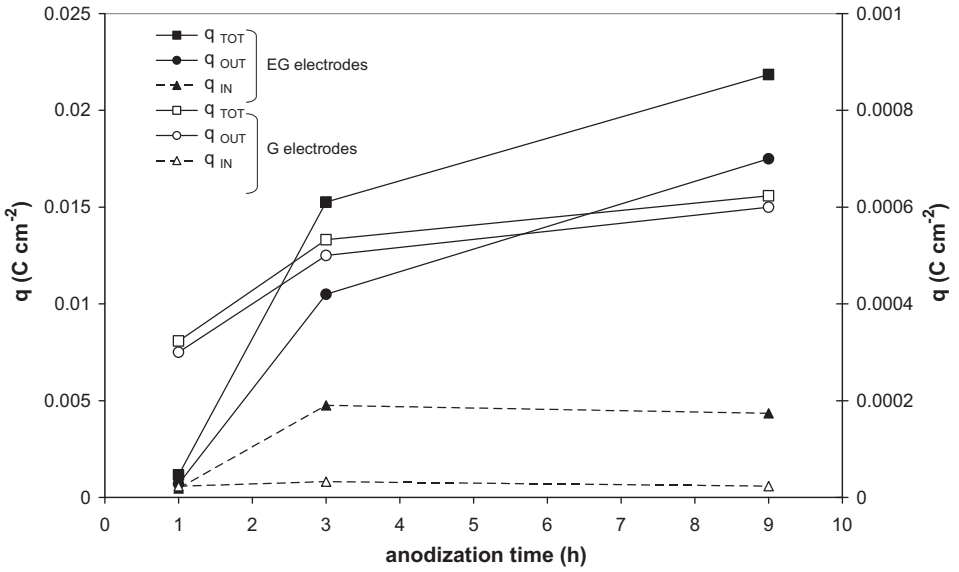

Fig. 4. Total, outer and inner charges for the considered electrodes as a function of the anodization time. Full symbols, primary axis: EG electrodes; empty symbols, secondary axis: G electrodes.

Table 3
circuit parameters obtained by fitting the experimental impedance results with the selected equivalent circuit.

Sample	Porous layer				Compact layer			
	R_p [Ω cm^2]	Q_p [F cm^{-2}]	n_p	τ_p [s]	R_c [Ω cm^2]	Q_c [F cm^{-2}]	n_c	τ_c [s]
G9								
Dark	716.80	0.23×10^{-2}	0.68	2.12	1.02×10^{5}	0.36×10^{-3}	1	36.57
λ = 380 nm	28.57	0.87×10^{-2}	0.34	1.6×10^{-2}	2.31×10^{4}	0.38×10^{-3}	0.91	10.87
EG9								
Dark	2.972	0.14×10^{-2}	0.70	4.0×10^{-4}	3.87×10^{4}	0.31×10^{-3}	0.93	14.79
λ = 380 nm					4484	0.45×10^{-3}	0.89	2.17

different concentration of defects in the two layers, may determine different values of resistance and capacity, and in turn different distribution of the charges and different depletion regions of each layer. So, different rates of the capacitive/resistive responses could be measured at the two layers: depending on the cases, they can be comparable each others or one prevailing over the other. Time constants ($\tau^n = Q \times R$), also reported in Table 3 as derived from the fit, can help to quantify the processes occurring at the two layers.

In the specific, if the time constants in porous and compact layers are compared, their very different values indicate that, especially at the EG9 sample, the process occurring at the compact layer is the controlling one. About five orders of magnitude are measured between the two time constants at EG9 in the dark, indicating a very rapid process at its porous layer, which is further accelerates under irradiation: in this case only one RQ element is sufficient to describe the behaviour of the sample, the resistance of the porous layer being enclosed in the initial R_1 value.

Lower differences are measured between the related time constants at G9 sample: less than two orders of magnitude separate the two constants so suggesting that for this sample the rates of the processes at the two layers are more comparable.

EIS data were also used to perform the Mott Schottky (MS) analysis [23]. The imaginary component of the impedance Z'' measured in a range from 100 kHz to 0.1 Hz allows to evaluate the capacity as $C = 1/(2\pi f Z'')$. Actually, when the semiconductor is under depletion conditions, the charge space capacitance varies with the potential following the equation:

$$\frac{1}{C_{SC}^2} = \frac{2}{\varepsilon_r \varepsilon_0 q N_D}\left((E_{appl} - E_{fb}) - \frac{kT}{q}\right) \quad (1)$$

were k is the Boltzmann constant, T the absolute temperature, q the electron charge, ε_0 the vacuum dielectric constant and ε_r the relative dielectric constant of TiO_2. Therefore, at least theoretically, the correlation between $1/C^2$ and the applied potential would exhibit a linear dependence. The intersection with the x axis represents the flat band potential, E_{fb}, whereas the donor density, N_D, can be calculated from the slope of this plot. However, when porous and defective structures are concerned, MS plot may show a wide variation of data with frequency [15,24], so making difficult the choice of the frequency value at which carry out the analysis.

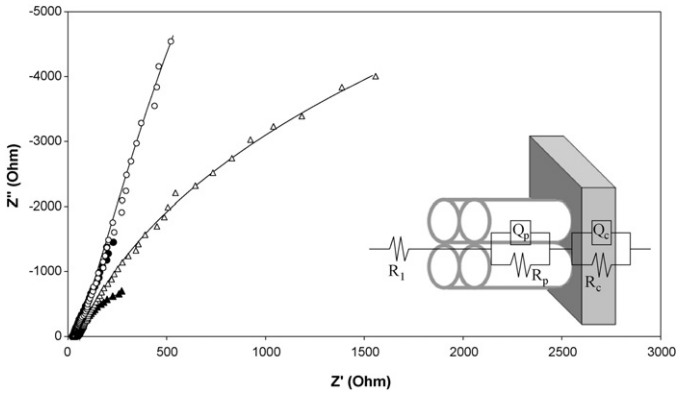

Fig. 5. EIS results for G9 (empty symbols) and EG9 (full symbols): Nyquist plots measured in the dark (triangles) and under irradiation at 380 nm (circles). Solid lines refer to the model fit. Data are measured at 0.4 V. Inset: schematic of the two layer structure and related equivalent circuit.

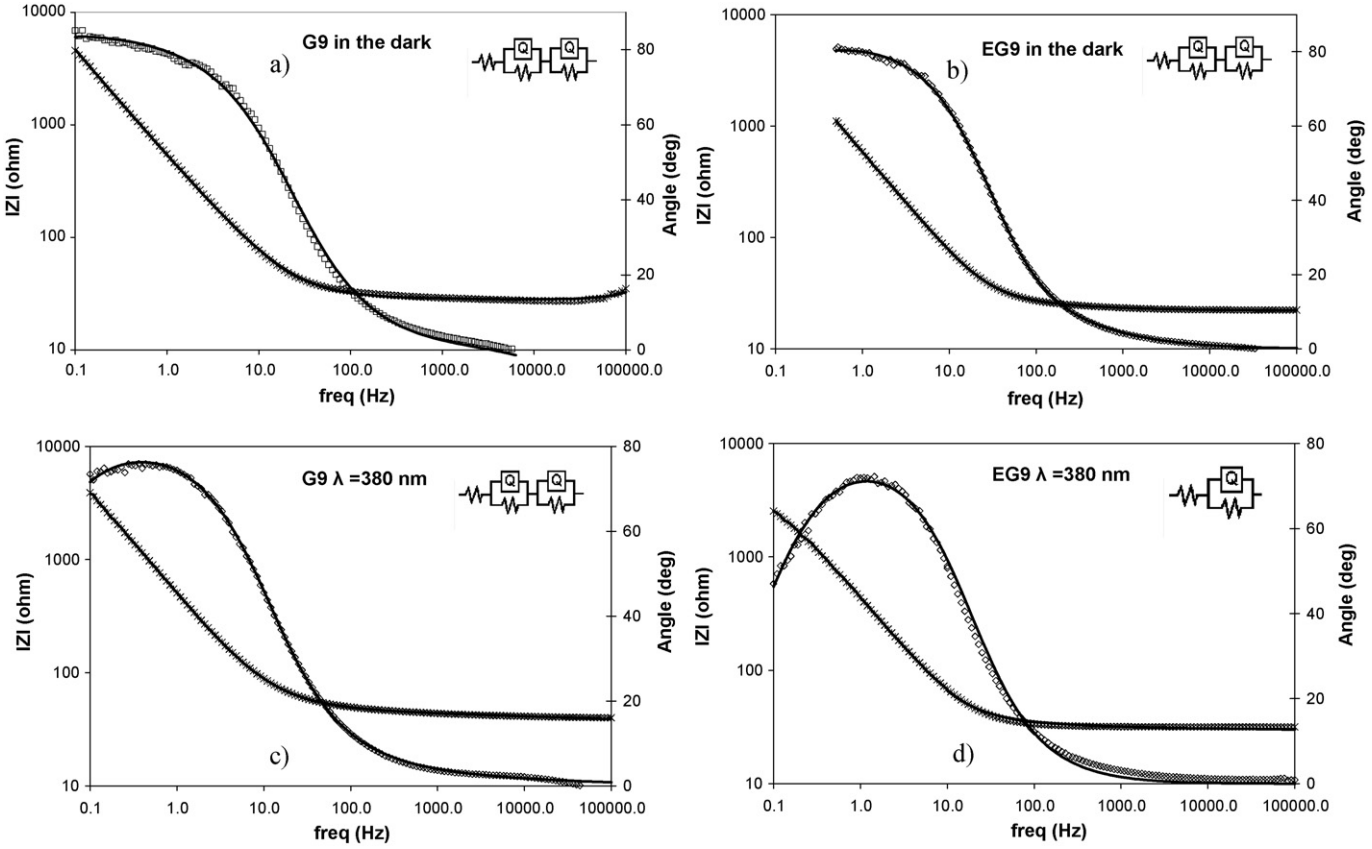

Fig. 6. EIS results for G9 and EG9: phase angle (empty symbols) and modulus (asterisks) Bode plots; solid lines refer to the model fit. Inset: equivalent circuit used for EIS data interpretation. (a) G9 in the dark, (b) EG9 in the dark, (c) G9 under irradiation, and (d) EG9 under irradiation. Data measured at 0.4 V.

Frequencies higher than 1 kHz are generally considered sufficient for Mott–Schottky analysis [25]: however, values of 3 Hz [15], 1000 Hz [11], or 3000 Hz [26], can be frequently met in the related papers in the literature.

In the present case, the N_D values for all the investigated electrodes are calculated at the frequencies of 3 and 3000 Hz. Some remarks may be made by comparing the values in Table 4: (i) G electrodes show higher N_D values than EG samples; (ii) anodization time does not seem to be very influential; (iii) for each sample, N_D calculated at 3 Hz are definitely higher than that evaluated at 3000 Hz: as pointed out in the introduction, as the frequency decreases defects with longer emptying time can be detected.

To investigate this last aspect, MS analysis was repeated for each frequency, and the obtained results for the samples G9 and EG9 are reported in Fig. 7.

N_D values always increasing with decreasing frequency are calculated as result of the increasing involvement of the slow-response defects that correspond to deeper energetic levels in the band gap. Moreover, data in figure show that the most important differences between G9 and EG9 are measured just at the lowest frequency.

Table 4
N_D values obtained at 3 and 3000 Hz for the investigated electrodes.

Sample	N_D at 3 Hz (cm^{-3})	N_D at 3000 Hz (cm^{-3})
G1	2.00×10^{23}	1.84×10^{22}
G3	6.71×10^{23}	2.44×10^{21}
G9	3.93×10^{23}	1.87×10^{22}
EG1	3.52×10^{20}	7.23×10^{19}
EG3	2.65×10^{20}	7.89×10^{19}
EG9	3.86×10^{22}	3.09×10^{21}

According to the results obtained from the equivalent circuit approach, the schematic representation of the nanotube structure as consisting of compact and porous layers, can explain these results. The comparison among the time constants associated to each layer, highlighted that at EG9 sample the controlling process is that occurring in the compact layer, resulting definitely slower than that in the porous layer (by five orders of magnitude in the dark). Therefore data reported for samples EG9 in Fig. 7 could be representative mainly of the compact layer response.

At the G9 sample the resistive/capacitive behaviour of the two layers results more comparable. Consequently, also a contribution of the porous layer could be present for this sample in Fig. 7, that should be visible at the highest frequencies, since fast and superficial states are expected to be dominant in this layer. Thus, the stronger difference of data at the lowest frequencies could indicate for G sample a higher density of defect in the compact layer or its greater thickness.

The same analysis was performed under light radiation, and the results are shown in Fig. 8. Data highlight how the larger effect of the light is exerted on the deeper sites, visible at the lower frequencies. Also in this case, due to its highly conducting character, the capacitive response of the porous layer is hardly evidenced.

The high increase of N_D at EG9 can indicate that surface states at the compact layer act as traps for the electrons generated during the irradiation. Due to the higher rate of growth of nanotubes a thinner compact layer may be present in EG9. Just this low thickness as well as the low N_D values may determine a limited effect of the potential. The depletion region could occupy the entire thickness of the layer so that the effect of the potential is not more able to liberate the trapped electrons that thus participate to the capacitive response of the layer.

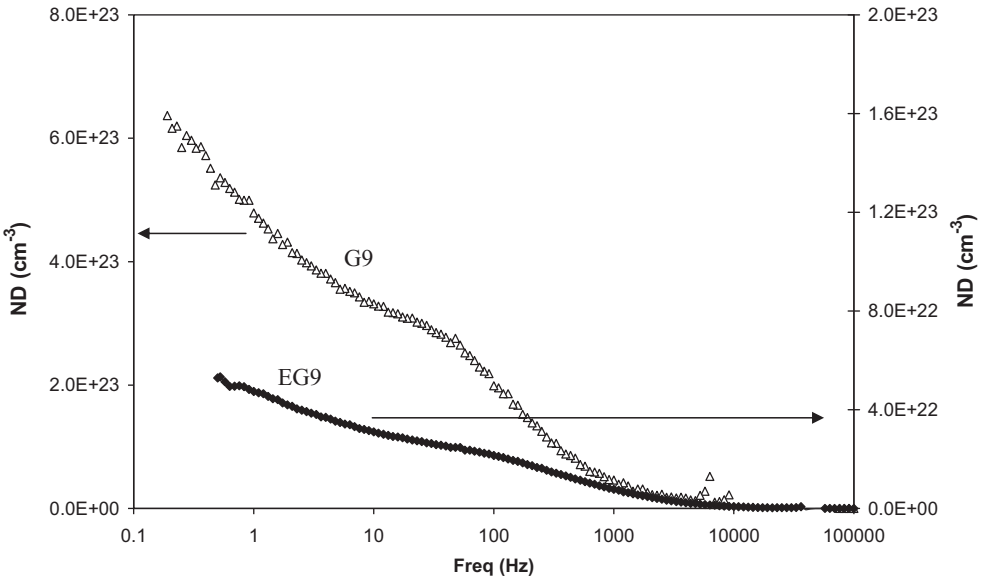

Fig. 7. N_D values vs frequency for samples G9 (empty symbols, primary axis) and EG9 (full symbols, secondary axis).

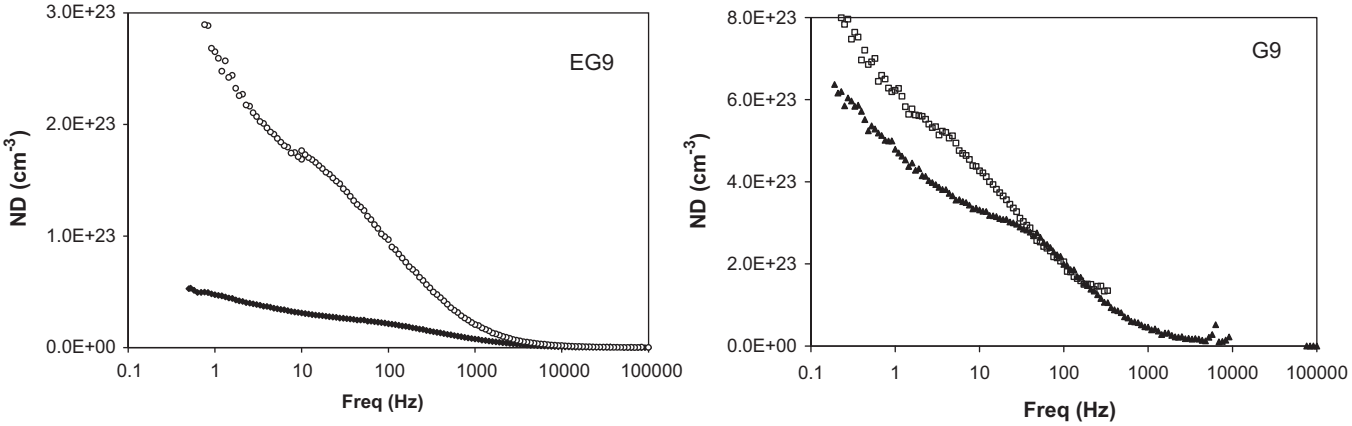

Fig. 8. N_D values vs frequency for samples EG9 and G9 in the dark (full symbols) and under irradiation (empty symbols).

The lower effect of the light on N_D values at G9 suggests a very strong effect of the potential on the photo-generated electrons that are continuously separated because the thickness of the compact layer is always able to support an increasing band bending.

These findings are in agreement with the shape of the photocurrents of each sample: at EG9 sample the photocurrent reaches in few millivolts the saturation, according to the fact that the potential is no more influent. On the contrary, at the G samples, the photocurrent trend always increasing with the potential is in agreement with the photo-induced charges being continuously separated by the potential.

4. Conclusions

The work shows an analysis of the photo-electrocatalytic behaviour of TiO_2 nanotube electrodes grown in different conditions. Results obtained suggest the complexity of the studied systems whose behaviour can be explained considering the schematic representation of the nanotube structures as consisting of two layers, compact and porous, behaving as two in series capacitors.

The porous layer is provided with higher surface and defectiveness, with a consequent higher electronic conductivity: its contribution is reflected in a quasi-nernstian dependence of photocurrent on the potential, with slope increasing as more extensive and defective is the layer.

In the studied samples the contribution of porous layers is visible in the quasi-linear slopes of photocurrents and confirmed by the circuital parameters: at samples EG, smaller value of R_p correspond to very high slopes in the first part of photocurrent curves; at samples G, higher R_p values correspond to lower slopes. This is in agreement with the related superficial areas of the porous layers.

The compact layer proves to be less defective and obviously with a lower surface area: its contribution is reflected in the saturation current, and depends on its thickness and defectiveness.

In the studied samples the contribution of compact layers is visible mostly in EG samples, where a too thin compact layer and/or the scarce defectiveness, lead to the saturation of photo-currents.

At samples G, in the investigated range of applied potential, the response of the system is mainly determined by the porous layer, and the photocurrent does not reach a saturation value.

It is clear that in order to achieve high performance in terms of photocurrent, both contributions are crucial. The porous layer should be as conductive as possible, and this can be achieved

enhancing the length of the nanotubes and thus their superficial area. At the same time, the thickness of the compact layer must be optimized to not limit the current and to not constitute a further resistance to the charge transport.

An engineered structure of the nanotubes is therefore necessary in order to achieve the best performance.

Acknowledgements

Ministero Italiano dell'Istruzione, dell'Università e della Ricerca and Belgian Federal Science Policy Office (BELSPO) through the "Mandats de retour" action, are gratefully acknowledged for the financial support. Ane Zabala is gratefully acknowledged for her contribution in the experimental activity.

References

[1] A. Fujishima, X. Zhang, D.A. Tryk, Surf. Sci. Rep. 63 (2008) 515–582.
[2] J.M. Macak, H. Tsuchiya, A. Ghicov, K. Yasuda, R. Hahn, S. Bauer, P. Schmuki, Curr Opin Solid State Mater 11 (2007) 3–18.
[3] K. Shankar, J.I. Basham, N.K. Allam, O.K. Varghese, G.K. Mor, X. Feng, M. Paulose, J.A. Seabold, K.S. Choi, C.A. Grimes, J. Phys. Chem. C 113 (2009) 6327–6359.
[4] Y.L. Kuo, T.L. Su, F.C. Kung, T.J. Wu, J. Hazard. Mater. 190 (1–3) (2011) 938–944.
[5] Y. Wanga, C. Fenga, M. Zhanga, J. Yanga, Z. Zhanga, Appl. Catal., B 104 (3/4) (2011) 268–274.
[6] M. Kitano, M. Takeuchi, M. Matsuoka, J.M. Thomas, M. Anpo, Catal. Today 120 (2007) 133–138.
[7] J. Nowotny, T. Bak, M.K. Nowotny, L.R. Sheppard, J. Phys. Chem. B 110 (2006) 18492–18495.
[8] P. Kofstad, Nonstoichiometry, Electrical Conductivity and Diffusion in Binary Metal Oxides, Wiley, New York, 1972.
[9] M.K. Nowotny, T. Bak, J. Nowotny, C.C. Sorrell, Phys. Status Solidi B 242 (2005) R88–R90.
[10] J. Nowotny, T. Bak, M.K. Nowotny, L.R. Sheppard, Int. J. Hydrogen Energy 32 (2007) 2651–2659.
[11] H. Tsuchiya, J.M. Macak, A. Ghicov, A.S. Rader, L. Taveira, P. Schmuki, Corros. Sci. 49 (2007) 203–210.
[12] S. Palmas, A.M. Polcaro, J. Rodriguez Ruiz, A. Da Pozzo, M. Mascia, A. Vacca, Int. J. Hydrogen Energy 35 (2010) 6561–6570.
[13] S. Palmas, A. Da Pozzo, M. Mascia, A. Vacca, A. Ardu, R. Matarrese, I. Nova, Int. J. Hydrogen Energy 36 (2011) 8894–8901.
[14] A.S. Jason, C. Kyoung-Shin, Chem. Mater. 23 (2011) 1105–1112.
[15] A.G. Muñoz, Electrochim. Acta 52 (2007) 4167–4176.
[16] F. Zhang, S. Chen, Y. Yin, C. Lin, C. Xue, J. Alloys Compd. 490 (2010) 247–252.
[17] S. Sreekantan, K.A. Saharudin, Z. Lockman, T.W. Tzu, Nanotechnology 21 (2010) 365603–365610.
[18] H. Yin, H. Liu, W.Z. Shen, Nanotechnology 21 (2010) 035601–35607.
[19] M. Park, A. Heo, E. Shim, J. Yoon, H. Kim, H. Joo, J. Power Sources 195 (2010) 5144–5149.
[20] H. Ishihara, J.P. Bock, R. Sharma, F. Hardcastle, G.K. Kannarpady, M.K. Mazumder, A.S. Biris, Chem. Phys. Lett. 489 (2010) 81–85.
[21] A.G. Muñoz, Q. Chen, P. Schmuki, J. Solid State Electrochem. 11 (2007) 1077–1084.
[22] R. Berenguer, C. Quijada, E. Morallon, Electrochim. Acta 54 (2009) 5230–5238.
[23] N. Sato, Electrochemistry at Metal and Semiconductor Electrodes, Elsevier, 1998.
[24] C. Da Fonseca, M. Guerreiro Ferreira, M. Da Cuhna Belo, Electrochim. Acta 39 (1994) 2197–2205.
[25] I. Hanzu, T. Djenizian, P. Knauth, J. Phys. Chem. C 115 (2011) 5989–5996.
[26] V.K. Mahajan, S.K. Mohapatra, M. Misra, Int. J. Hydrogen Energy 33 (2008) 5369–5374.